Miniaturized UWB Filters Integrated With Tunable Notch Filters Using a Silicon-Based Integrated Passive Device Technology

Zhengzheng Wu, *Student Member, IEEE*, Yonghyun Shim, *Student Member, IEEE*, and Mina Rais-Zadeh, *Member, IEEE*

***Abstract*—This paper reports on the implementation of miniaturized ultra-wideband filters integrated with tunable notch filters using a silicon-based integrated passive device technology. An ultra-wideband bandpass filter is realized on a micromachined silicon substrate, showing an insertion loss of 1.1 dB, return loss of better than 15 dB, and attenuation of more than 30 dB at both lower and upper stop-bands, with a spurious-free response up to 40 GHz. The filter occupies only 2.9 mm $\times$ 2.4 mm of die area. To address the in-band interference issues associated with ultra-wideband communication, very compact tunable notch filters are monolithically integrated with the bandpass filters. A two-pole tunable notch filter integrated with an ultra-wideband filter provides more than 20 dB rejection in the 5–6 GHz range to reject U-NII interferences, with a total footprint of 4.8 mm $\times$ 2.9 mm. The power handling, linearity, and temperature stability of filters are characterized and presented in this paper.**

***Index Terms*—Integrative passive devices (IPDs) and modules, interference suppression, MEMS or microelectromechanical systems, tunable filters, ultra-wideband.**

I. Introduction

ULTRA-WIDEBAND (UWB) has emerged as a fast growing technology since the Federal Communications Commission (FCC) approved the unlicensed use of the frequency spectrum from 3.1 to 10.6 GHz [1]. The allocated wide spectrum enables Impulse Radio-UWB (IR-UWB), which is based on transmitting and detecting short duration pulses. In contrast to narrowband systems, IR-UWB is carrier-less, greatly simplifying the RF front-end by using all-digital transmitters [2], [3] and receivers that do not require power hungry RF oscillators or PLLs [4], [5]. The low-cost and energy-efficient IR-UWB scheme is a good candidate for several applications, such as wireless sensor networks and handheld devices.

UWB communication stimulates both opportunities and challenges in the design and implementation of fully integrated RF front-ends [2]–[6]. Still, a major impediment to the wide adoption of UWB technology is the issue of narrowband interferences that might exist in the same frequency range. The FCC-regulated low UWB emission power (-41.3 dBm/MHz) necessitates interference mitigation techniques. Circuit design techniques, such as frequency selective receivers, have been explored to reject the interferences using active filters, but at the cost of increased CMOS chip area and higher power consumption [7], [8]. Alternatively, RF front-ends exploiting only subbands of the UWB frequency range have been used to address the interference issue [9], [10], although with reduced communication capacity. It is known that RF preselect filtering greatly relaxes the receiver linearity requirement and reduces the gain desensitization due to strong interferers. Also, for IR-UWB, filters used in transmitters can regulate the emission power of short duration pulses to comply with the FCC spectral mask and eliminate the use of additional pulse shaping circuits as in [11]. Therefore, low-loss, highly selective, and integrated passive UWB filters are needed.

So far, reported works have focused on UWB filter miniaturization based on microstrip, coplanar waveguide (CPW), or quasi-lumped components on low-loss microwave substrates such as FR4, LTCC, or LCP [12]–[19]. These filter implementations are developed mostly as standalone components. Our recent work demonstrated, for the first time, low-loss and miniaturized UWB filters fully integrated with fixed notch filters on silicon substrates using an integrated passive devices (IPD) technology [20]. In this paper, the proposed IPD technology is employed to fabricate UWB filters integrated with RF microelectromechanical system (MEMS) tunable notch filters. The tunable notch filters in this work are some of the most compact filters reported [21]–[28] that provide interference rejection of more than 20 dB (in 4.9–6.5 GHz frequency range) and low passband loss. Integration of UWB filters with tunable notches allows detect-and-avoid (DAA) mechanism, which can address the issue of interferences. Using the multiband orthogonal frequency division multiplexing (MB-OFDM), the DAA-enabled UWB radio can form the basis for cognitive radio implementation [29].

In this paper, first the IPD technology will be introduced. Then, the UWB and tunable notch filter design techniques that achieve size miniaturization and high-performance filtering will be discussed. Finally, integration result of the UWB filter with the tunable notch filter will be presented and characterization results of filters will be discussed. The presented filter technology is suitable for flip-chip assembly or multi-chip-module (MCM) integration with CMOS ICs, making the implementation of highly integrated UWB RF front-end modules realizable.

Manuscript received September 26, 2011; revised November 07, 2011; accepted November 18, 2011. This work was supported in part by the National Science Foundation under Award 1055308 and in part by the University of Michigan, Ann Arbor.

The authors are with the University of Michigan, Ann Arbor, MI 48109 USA (e-mail: zzwu@umich.edu; minar@umich.edu).

Color versions of one or more of the figures in this paper are available online at http://ieeexplore.ieee.org.

Digital Object Identifier 10.1109/TMTT.2011.2178428

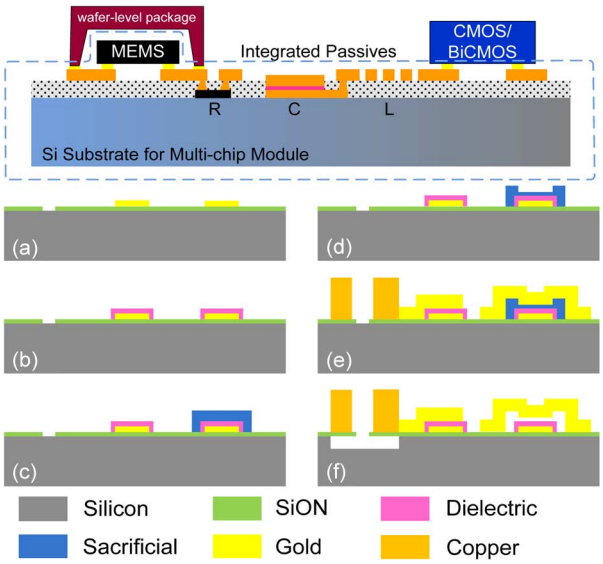

Fig. 1. Conceptual view of the IPD multi-chip integration (top) and the process flow of the IPD technology (bottom).

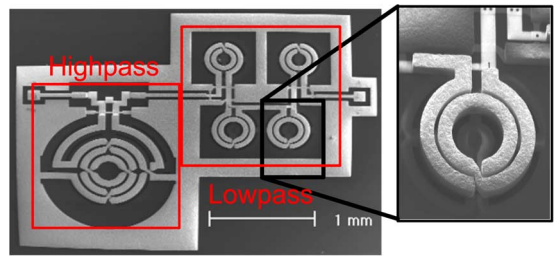

Fig. 2. A SEM image of a cascaded bandpass filter on a micromachined substrate (size: 2.9 mm × 2.4 mm). Inset shows the inductor on a SiON membrane.

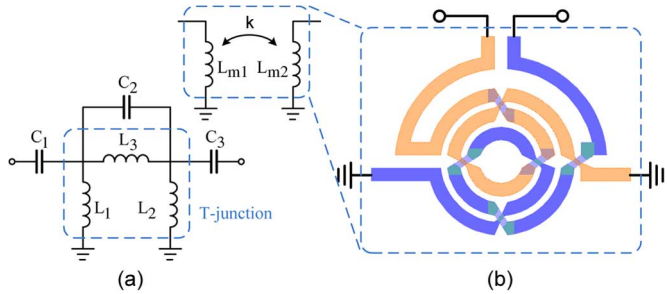

Fig. 3. (a) High-pass filter circuit, and (b) layout of coupled inductors.

II. Fabrication Process Flow of the Integrated Passive Device (IPD) Technology Platform

The UWB filters are fabricated using a silicon-based IPD technology, schematically shown in Fig. 1 (top). Using this process, RF MEMS tunable capacitors, switches, and high-Q inductors can be simultaneously fabricated. When wafer-level packaged, the all-in-one IPD is expected to offer a more compact form factor and a lower cost passive integration scheme compared to other RF MEMS technologies.

The fabrication process is shown in Fig. 1. The process starts with the deposition of a 2 μm-thick low-stress silicon oxynitride (SiON) dielectric layer on a high-resistivity ($> 1\ \mathrm{k\Omega \cdot cm}$) silicon substrate. The processing steps are: (a) deposition and patterning of gold as the bottom electrode; (b) deposition of a dielectric layer for metal-insulator-metal (MIM) capacitors; (c) deposition and patterning of an amorphous silicon sacrificial layer; (d) etching the sacrificial layer to form a step for realizing high tuning ratio MEMS tunable capacitors and ohmic-contact dimples; (e) gold electroplating for the top metal electrode of MIM capacitors; (e) thick copper electroplating to form high-Q inductive components; and (f) xenon difluoride gaseous etching of the amorphous silicon to form air-gap membrane, and selectively removing the silicon substrate to reduce the substrate loss. Where the silicon substrate is partially removed, the SiON dielectric membrane provides support for metal structures for enhanced mechanical robustness. The sacrificial layer step etch allows the formation of dual gaps for high analog tuning range (>4:1) MEMS capacitors [30], [31], and contact dimples used in ohmic-contact MEMS switches [32].

III. Design and Implementation of Filters

Using the presented IPD platform, UWB bandpass filters as well as tunable planar notch filters are demonstrated. Filters are designed in co-planar configuration with proximate ground plane so that the electromagnetic field is confined on the surface of the substrate. Therefore, the performance of filters is not affected by backside metallization, variations in the substrate thickness, or the packaging layer.

To accurately predict parasitic effects of the co-planar filter configuration, filters are simulated using the HFSS full-wave electromagnetic simulation tool [33]. In all HFSS simulations, the conductivity of electroplated copper is taken as $4.9 \times 10^7\ \mathrm{S/m}$ and the loss tangent and conductivity of the silicon substrate are assumed to be 0.004, and $1\ \mathrm{k\Omega \cdot cm}$, respectively. In the following subsections, the design strategy of the UWB filters, tunable notch filters, and UWB filter with an integrated tunable notch will be discussed, and the simulation results of the filters will be compared with measured results.

A. Cascaded UWB Bandpass Filter

Previously we reported on a UWB bandpass filter design composed of a cascade of low-pass and high-pass filter sections that offers low loss on both micromachined and solid silicon substrates (Fig. 2) [20]. The filter networks were synthesized from generalized Chebyshev configuration [34], providing steep rejection with a low-order design. Fig. 3(a) shows the circuit diagram of the high-pass filter section. From the filter synthesis and optimization, the value of the components for the high-pass filter having a cutoff frequency of 3.1 GHz and out-of-band rejection of 30 dB below 2 GHz can be obtained. The derived filter network contains a high-value inductor, L_3, in the T-junction, which can be eliminated by transforming the T-junction into a pair of mutually coupled inductors [35]. The component values of the coupled inductor pair are listed in Table I.

Mutual coupling (k) of 0.2 is difficult to implement using either tightly coupled interleaved structures [36] or loosely coupled proximate inductor pairs. Therefore, a custom-designed inter-winded inductor pair is used [Fig. 3(b)]. The inter-winded pair has tight coupling in the inner turns and weak coupling in

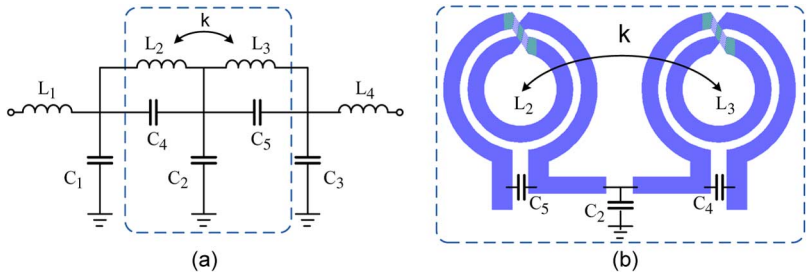

Fig. 4. (a) Low-pass filter circuit and (b) layout of the coupled inductor pair.

TABLE I
COMPONENTS IN THE HIGH-PASS FILTER

C_1 (C_3)	C_2	L_1 (L_2)	L_3	L_{m1} (L_{m2})	k
1.04 pF	0.825 pF	2.21 nH	8.83 nH	1.84 nH	0.2

TABLE II
COMPONENTS IN THE LOW-PASS FILTER

C_1 (C_3)	C_2	C_4 (C_5)	L_1 (L_4)	L_2 (L_3)	k
0.361 pF	0.275 pF	1 pF	0.77 nH	1 nH	0.08

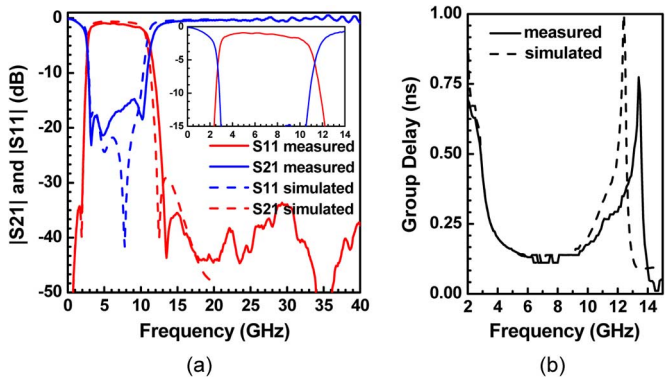

Fig. 5. Measured response of the cascaded high-pass–low-pass bandpass filter on a micromachined substrate (silicon is removed beneath inductors). (a) Insertion loss and return loss (with closed-up view of passband performance inset). (b) Group delay.

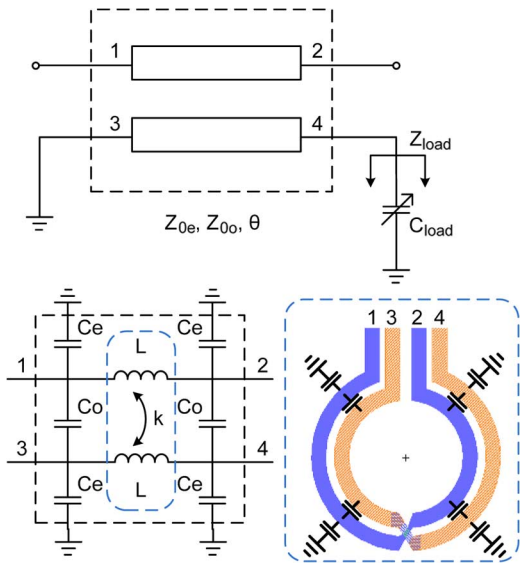

Fig. 6. Circuit implementation of the notch filter.

the outer turns of the inductors, offering the desired mutual coupling of 0.2. The relatively small size of these mutually coupled inductors is the main contributing factor in significant size reduction of the high-pass filter.

The circuit diagram of the low-pass filter section of the UWB filter is shown in Fig. 4(a). Inductors L_2 and L_3 are purposefully coupled by placing them in close proximity, as depicted in Fig. 4(b). As a result, the transmission zero is moved close to the passband to improve the roll-off at the edge of the high-frequency cutoff. The component values used in the low-pass filter are listed in Table II. It can be seen that the substrate parasitic capacitances in the filter can be absorbed into filter components C_1, C_2, and C_3, making it possible to achieve a low-loss filter at frequencies up to 10 GHz [20]. Fig. 5 shows the measured and simulated responses of a cascaded (high-pass–low-pass) UWB bandpass filter on a micromachined silicon substrate. The cascaded UWB filter has a bandwidth of 7.6 GHz (3–10.6 GHz) within which the return loss is better than 15 dB. The mid-band insertion loss of the filter is 1.1 dB (at 6.85 GHz). This filter exhibits an excellent out-of-band rejection of at least 30 dB at lower (<2 GHz) and upper (>13 GHz) sides of the passband. A spurious-free response up to 40 GHz is obtained. The group delay is less than 0.25 ns.

B. Tunable Notch Filter

UWB communication using bandpass filters in the receiver may suffer from strong in-band interferers. The center frequencies of in-band interferences may not be known in advance. Considering the IEEE 802.11a interferers, for example, narrowband interferers can appear in a range of 4.9–5.85 GHz. Therefore, a fixed notch filter cannot completely resolve the interference problem of UWB filters. It is also necessary that notch filters have sufficient rejection level across the communication band of interferers. As such, analog tuning of a notch filter with high rejection level is required to block unknown interferers. Reported works have been focused on the design of fixed-frequency narrowband notch filters embedded with UWB bandpass filters [12], [16]–[18], [20]. In this paper, we demonstrate tunable notch filters that can be monolithically integrated with UWB filters to mitigate the interference issue.

The design of miniaturized notch filters in this work is based on the configuration of coupled transmission line bandstop filters [37]. As can be seen in Fig. 6, the first-order notch filter cell is obtained by loading a pair of coupled transmission lines with a capacitor for reduced electrical length. If the even-mode and

odd-mode impedances (Z_{0e} and Z_{0o}) of a coupled line are designed to match the port impedance Z_0 ($Z_0 = 50\ \Omega$), i.e.,

$$Z_0 = \sqrt{Z_{0e} Z_{0o}} \tag{1}$$

the four-port S-parameter matrix $[S]$ of a pair of symmetrical coupled transmission line with electrical length θ can be written as [38]

$$[S] = \begin{pmatrix} 0 & \alpha & \beta & 0 \\ \alpha & 0 & 0 & \beta \\ \beta & 0 & 0 & \alpha \\ 0 & \beta & \alpha & 0 \end{pmatrix} \tag{2}$$

where

$$\alpha = \sqrt{1 - C^2}/(\sqrt{1 - C^2}\cos\theta + j\sin\theta), \tag{3}$$

$$\beta = jC\tan\theta/(\sqrt{1 - C^2} + j\tan\theta). \tag{4}$$

C is the coupling coefficient defined as

$$C = (Z_{0e} - Z_{0o})/(Z_{0e} + Z_{0o}). \tag{5}$$

When Port 3 is grounded, the reflection coefficient at Port 3 is

$$\Gamma_{L3} = -1. \tag{6}$$

Further, when Port 4 is terminated with impedance $Z_{\rm load}$, the reflection coefficient at Port 4 is

$$\Gamma_{L4} = (Z_{\rm load} - Z_0)/(Z_{\rm load} + Z_0). \tag{7}$$

With these terminations on Ports 3 and 4, the coupled line becomes a two-port network with S-parameters of

$$S_{11} = -S_{22} = -\frac{\beta^2}{1 + \alpha^2\Gamma_{L4}}, \tag{8}$$

$$S_{21} = -S_{12} = \alpha\left(1 - \frac{\beta^2\Gamma_{L4}}{1 + \alpha^2\Gamma_{L4}}\right). \tag{9}$$

When there is an ideal capacitive load ($C_{\rm load}$) terminating Port 4, the two-port network is a bandstop network. By solving $|S_{21}| = 0$, the notch center frequency, ω_0 can be found.

$$\omega_0 C_{\rm load} Z_0 \tan\theta = \sqrt{1 - C^2}. \tag{10}$$

The bandwidth of the notch filter can be found from (8)–(10). For example, the -10 dB bandwidth of S_{21} can be obtained by solving $20 \times \log(|S_{21}|) = -10$ dB. The -10 dB fractional bandwidth versus notch center frequency is plotted in Fig. 7 for various electrical lengths (θ) and coupling coefficients (C).

To further reduce the filter size, the coupled transmission line section is transformed into a lumped LC coupler [39], as seen in Fig. 6. Using this lumped transformation, narrowband notch filters can be designed using low-value inductors, making it possible to achieve high-Q, small size, and improved filter shape compared to conventional bandstop LC filters [21]–[23]. Although the lumped conversion is in principle a narrowband approximation of the coupled transmission line configuration, the converted lumped network has low passband insertion loss up to very high frequencies. In designing the lumped coupled inductors, parasitic capacitors need to be taken into account as part of the even-mode (C_e) and odd-mode capacitances (C_o), as depicted in Fig. 6. A lumped notch filter is transformed from a coupled line filter with electrical length (θ) of 31.5° at 5.25 GHz and coupling coefficient (C) of 0.51, which results in a pair of inductors with inductance of 0.93 nH and mutual coupling coefficient (k) of 0.51 (Table III). If a tunable capacitor ($C_{\rm load}$) with tuning range from 0.4 to 1.8 pF is used, the notch center frequency can be tuned from 7 to 3.7 GHz. The expected frequency tuning as well as the -3 and -10 dB fractional bandwidths across the tuning range is plotted in Fig. 8.

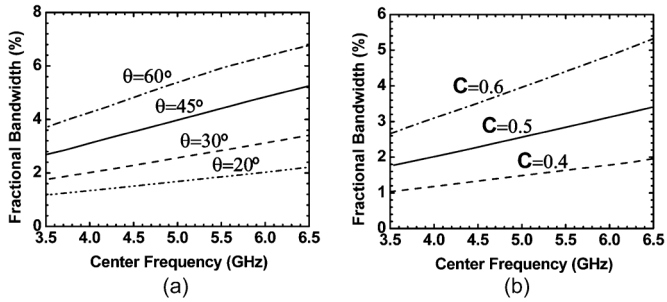

Fig. 7. Fractional bandwidth (-10 dB) of the notch filter versus center frequency. (a) Different electrical lengths (θ) at 5.25 GHz, coupling coefficients (C) = 0.5. (b) Different C values, $\theta = 30°$ at 5.25 GHz.

TABLE III
COMPONENT VALUES OF THE TUNABLE NOTCH FILTER

L	k	C_e	C_o
0.93 nH	0.51	98 fF	100 fF

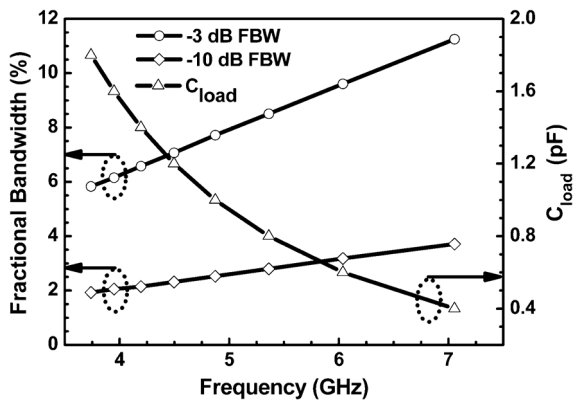

Fig. 8. Fractional bandwidth and load capacitance ($C_{\rm load}$) of the lumped notch filter versus center frequency.

Dual-gap MEMS tunable capacitors are utilized to achieve continuous frequency tuning. As can be seen in the SEM image and cross-sectional view shown in Fig. 9, the narrow center gap defines the tunable RF capacitor ($C_{\rm MEMS}$), while the wider side-gap is used for electrostatic actuation. This configuration overcomes the pull-in effect of electrostatic actuators [30]. A fabricated dual-gap MEMS capacitor is tuned from 0.38 to 2.1 pF (5.5:1) when measured at 500 MHz (Fig. 9). The equivalent circuit model of the RF MEMS tunable capacitor is plotted in Fig. 9, and the equivalent component values are

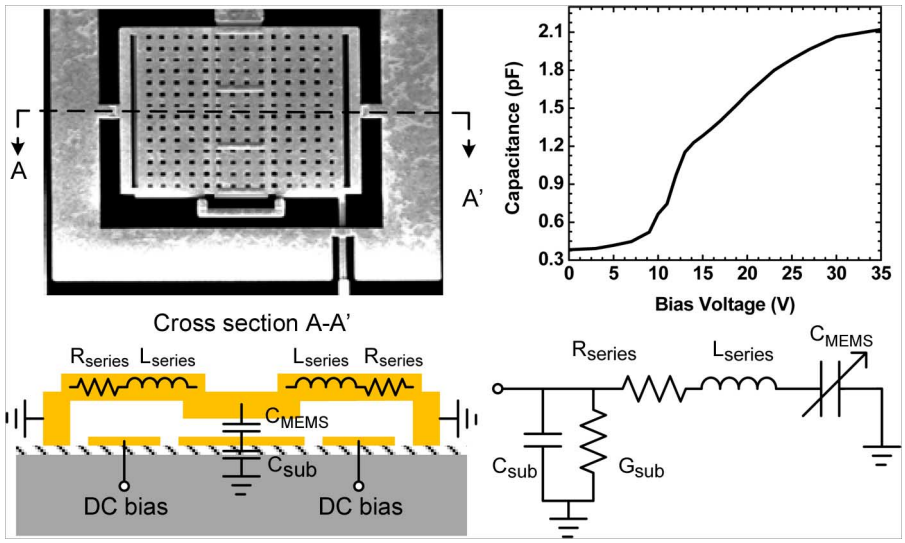

Fig. 9. A SEM image, measured tuning results, cross-sectional view, and circuit model of a fabricated dual-gap MEMS capacitor.

TABLE IV
COMPONENT VALUES IN THE MEMS CAPACITOR MODEL

C_{MEMS}	L_{series}	R_{series}	C_{sub}	G_{sub}
0.38-2.1 pF	130 pH	0.36 Ω	55 fF	30 kΩ

TABLE V
PARAMETERS OF DUAL-GAP MEMS CAPACITOR

DC actuation area	270×70×2 μm^2
RF capacitor area	260×70 μm^2
Initial DC actuation air gap (g_{DC0})	2 μm
Initial RF air gap (g_{RF0})	0.4 μm
Spring constant (k)	36 N/m
Mechanical Q	1
Resonance frequency (f_0)	9 kHz

given in Table IV. The design of the MEMS capacitors involves several tradeoffs among various parameters including Q, tuning voltage, linearity, and tuning speed [31]. The most important parameter depends on the application and the capacitor design may be optimized to achieve a specific goal.

There is no stringent requirement on the tuning speed of the notch filter if the existing interferences do not change frequently. Therefore, continuously tuned MEMS capacitors that offer a tuning speed on the order of 100 μs seems reasonable for the filter design. Low tuning bias voltage is preferred as it reduces the power consumption of DC converters and simplifies the implementation of the tuning bias circuit. However, a capacitor with low tuning bias suffers from insufficient power handling capability, as will be discussed in Section IV. The designed parameters of the RF MEMS tunable capacitor used in the tunable notch filter are summarized in Table V.

As can be seen in Fig. 6, the RF MEMS tunable capacitor forms a series LC resonator in the notch filter. Also, the MEMS tunable capacitor has a series parasitic inductance, L_{series} (see Fig. 9). The parasitic inductance of the MEMS capacitor is absorbed into the main inductor of the tank. Therefore, the Q of the MEMS capacitors is improved at high frequencies and the

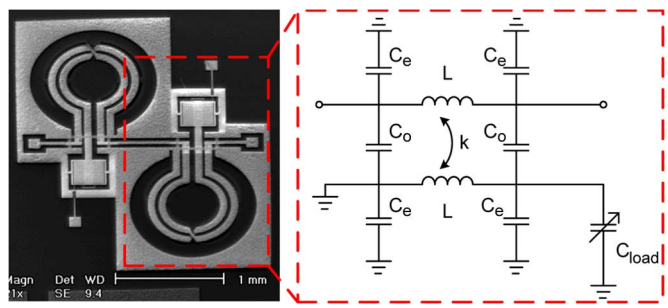

Fig. 10. A SEM image of a fabricated two-pole tunable notch filter together with the circuit schematic of the tunable notch filter cell.

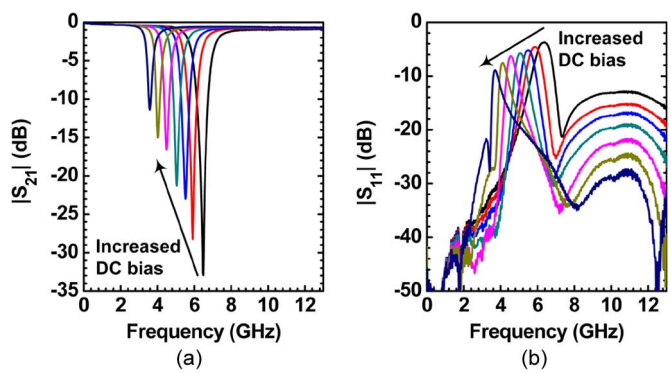

Fig. 11. Measured tuning characteristics of a two-pole tunable notch filter. (a) Insertion loss. (b) Return loss at different bias levels.

usable frequency range of the device is extended beyond the self-resonant frequency predicted by the conventional extraction method using Z-parameters: $|imag(Z_{12})|/real(Z_{12}) = 0$. A two-pole tunable notch filter is realized by cascading two first-order notch cells (Fig. 10). The measured tuning characteristic of the two-pole notch filter is shown in Fig. 11. A tuning range of 3 GHz (6.5–3.5 GHz) is achieved by applying a DC bias voltage up to 17 V to the MEMS capacitors. The tunable notch filter maintains low passband loss (<1 dB) up to 13 GHz at all tuned states.

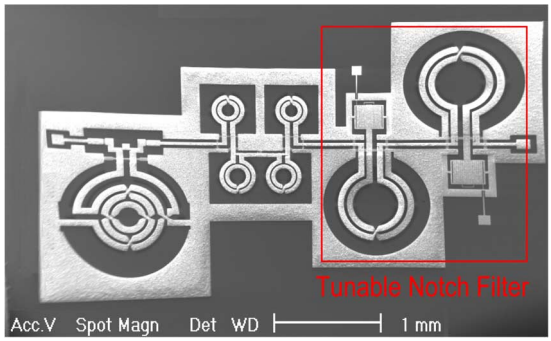

Fig. 12. A SEM image of the fabricated UWB filter integrated with a two-pole tunable notch filter (overall size: 4.8 mm × 2.9 mm).

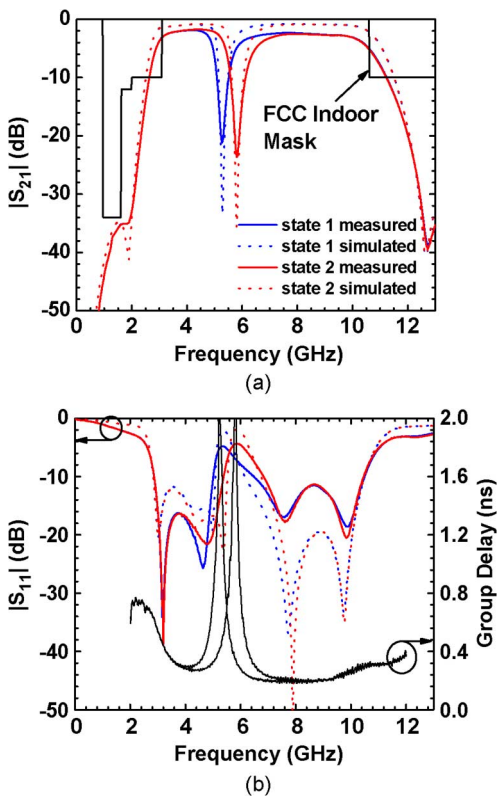

Fig. 13. Measured and simulated responses of the UWB bandpass filter integrated with a two-pole tunable notch filter (State 1: notch center at 5.25 GHz; State 2: notch center at 5.8 GHz). (a) Insertion loss. (b) Return loss and group delay.

C. UWB Filters With Integrated Notch Filters

The two-pole tunable notch filter is cascaded with UWB bandpass filters to allow in-band interference rejection capability in a DAA fashion (Fig. 12). Measured and simulated frequency responses of the filter at two tuning states are shown in Fig. 13. The two states are set to reject the interferences from 802.11a, at either the IEEE 802.11a lower band (5.15–5.35 GHz) or the higher band (5.725–5.825 GHz). The measured rejection level of the tunable notch filter is better than 20 dB covering the 5–6 GHz Unlicensed National Information Infrastructure (U-NII) band. The UWB passband insertion loss is less than 2.7 dB. The size of the UWB filter integrated with the two-pole tunable notch filter is 4.8 mm × 2.9 mm (Fig. 12).

The FCC indoor mask is overlapped on the filter responses in Fig. 13. Although the current design does not fully satisfy the FCC mask, compliance to FCC mask can be met by slightly reducing the filter bandwidth to account for the brick wall passband transition [15]. Table VI compares the tunable filters in this work with other recently reported works. As highlighted in the table, the filters implemented in this work achieve a significant size reduction (of 10×) with a competitive performance. Also, monolithic tunable UWB filters are for the first time realized in a silicon IPD technology.

IV. Filter Linearity and Temperature Stability

In addition to small-signal performance, power handling and linearity are also important performance metrics for tunable RF filters. The RF signal that passes through RF MEMS devices has an effective DC bias and causes self-actuation. As a result, at higher RF powers, the tuning range of the MEMS capacitor will be limited [30], [40]. In addition, intermodulation signals are generated due to the nonlinearity of MEMS devices [41], [42]. It should be noted that the AC voltage swing across the MEMS capacitor in a tunable LC circuit is amplified by the Q of the tank. Therefore, estimation of the power handling and linearity performance is essential when designing tunable filters.

A. Power Handling

The power handling of the MEMS capacitor is limited to an RF power level that causes the membrane to pull-in [41]. The maximum RF voltage that can be applied to a dual-gap MEMS capacitor at various DC bias before pull-in is analyzed in [30]. For the designed dual-gap MEMS capacitor of Fig. 9, the maximum tolerable RF voltage swing (peak-to-peak voltage) versus center frequency of the designed notch is plotted in Fig. 14. As can be seen, the maximum allowed RF voltage swing is larger than 1.6 V if the notch filter is tuned to frequencies above 5 GHz. Therefore, the tunable notch filter in this work is suitable for UWB receivers. Higher power handling can be achieved by increasing the stiffness of the RF MEMS capacitors at the cost of increased DC bias.

B. Linearity

To study the linearity performance of the fabricated tunable notch filter, a nonlinear model is developed for the MEMS capacitor using the method discussed in [42]. Modifications are made to accurately reflect the dual-gap configuration as well as the separate DC bias and RF electrodes using the device characteristics summarized in Table V. The capacitor model is then included in the two-pole tunable notch filter to predict the linearity and the large signal behavior. The two-pole notch filter is tuned to 5.25 GHz, a typical tuning state to reject the interference from WLAN. Agilent ADS [43] Harmonic Balance simulation is used to predict the filter large signal behavior. In simulations, two-tone signals are applied to the notch filter with center frequency of 5.25 GHz, frequency offset of 1 kHz, and input power of −10 dBm (amplitude of 0.1 V across a 50 Ω termination). Because of the high resonator Q, the voltage swing at 5.25 GHz across the tunable capacitor is amplified to more

TABLE VI
COMPARISON OF UWB FILTERS WITH NOTCH

	Sharman [16]	Hao [17]	Luo [18]	Arachchige [19]	Previous Work [20]	This Work
Technology	Single layer PCB	Multilayer LCP	PCB (Hybrid Microstrip/CPW)	Multilayer LCP with GaAs varactors	Silicon IPD with micromachined substrate	Silicon IPD integrated with RF MEMS
Filter Size	22.2mm × 15.1mm	37.6 mm × 8 mm	16.2mm × 12.6 mm	N/A	**4.6 mm × 2.9 mm**	**4.8 mm × 2.9 mm**
In-Band Insertion Loss (dB)	< 0.7 dB at center of sub-passband	0. 16 dB at 4.28 GHz; 0.54 dB at 7.08 GHz; 0.75 dB at 9.53 GHz	0.69 dB at lower 1.49 dB at middle 0.63 dB at upper	N/A	1.8 dB at lower 2 dB at higher	1.8 dB at lower 2.6 dB at higher
Group Delay (ns)	~ 0.5 ns at center of sub-passband	0.4 ns at 4.28 GHz; 0.14 ns at 7.08 GHz; 0.54 ns at 9.53 GHz	< 0.59 ns; < 0.36 ns variation	N/A	< 0.3 ns	< 0.3 ns
Wide Stopband	No	Yes	10.3-15.1 GHz	N/A	**Up to > 40 GHz**	**Up to > 40 GHz**
Notched-band and Rejection	32 dB at 6.6 GHz	26.4 dB at 6.4 GHz; 43.7 dB at 8.0 GHz	21.9 dB at 5.23 GHz; 24.0 dB at 5.81 GHz	N/A	23 dB @ 5.28 GHz	21 dB at 5.25 GHz; 23 dB at 5.8 GHz;
Notch Tuning	fixed	fixed	fixed	Tunable: 4.5-6.5 GHz	fixed	**Tunable: 3.5-6.5 GHz**

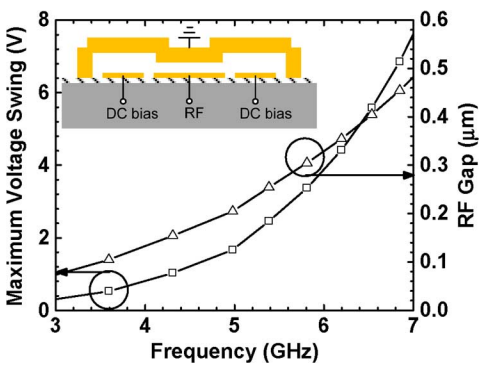

Fig. 14. Maximum allowed RF voltage swing (peak-to-peak voltage) of the notch filter.

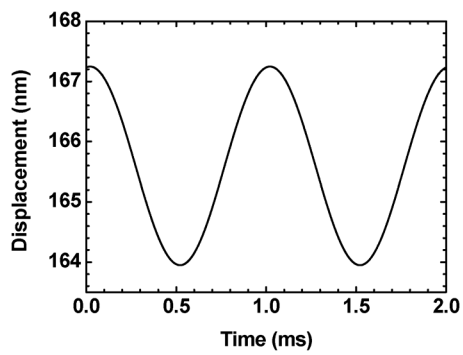

Fig. 15. Displacement of the tunable capacitor membrane at input power of −10 dBm.

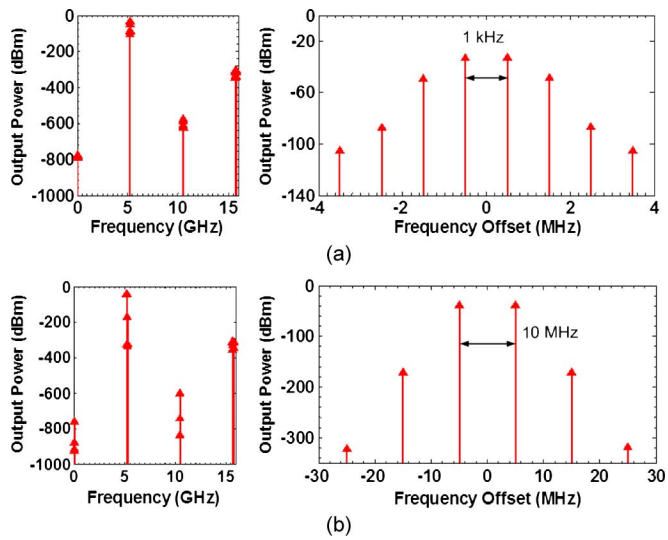

Fig. 16. Output spectrum with input offset of (a) 1 kHz and (b) 10 MHz.

than 0.5 V peak-to-peak. The displacement of the MEMS capacitor membrane under such two-tone input power is plotted in Fig. 15. As shown, the displacement fluctuation of the MEMS capacitor membrane under such high voltage swing (0.5 V) is less than 3.5 nm. This is due the fact that the membrane has a mechanical resonant frequency of less than 10 kHz (Table V). The low-pass mechanical response of the MEMS device significantly attenuates the high-frequency membrane vibration. The observed membrane movement is a response to the intermodulations that generate a signal tone at 1 kHz and excite the capacitor membrane through electrostatic force in the RF gap. When applying two-tone signals with larger frequency offsets (>10 kHz), the frequency of the intermodulation tone is beyond the mechanical resonant frequency of the membrane and even smaller vibration is expected.

Based on two-tone Harmonic Balance simulations, the output spectrum of the UWB filter integrated with tunable notch filter is plotted in Fig. 16. The two-pole notch filter is tuned to 5.25 GHz when the two-tone inputs have a center frequency of 5.25 GHz and input power of −10 dBm. In Fig. 16(a) and (b), two-tone inputs with a frequency offset of 1 kHz and 10 MHz are applied, respectively. It can be observed that there is higher harmonic output power around 5.25 GHz when two-tone inputs have 1 kHz offset. However, such inter-modulation tones are within the stopband of the notch filter, and they do not cause additional interference to the UWB passband. As can be observed in Fig. 16(b), when the frequency offset of the two-tone input (10 MHz) is far beyond the mechanical resonant frequency of the MEMS capacitor (i.e., 9 kHz), the intermodulation signals are highly attenuated. Therefore, very low harmonic output power is observed. It can be also found that very low-power intermodulation tones are observed across the entire UWB passband (Fig. 16). The notch filter nonlinearity does not produce additional interferences to the UWB passband.

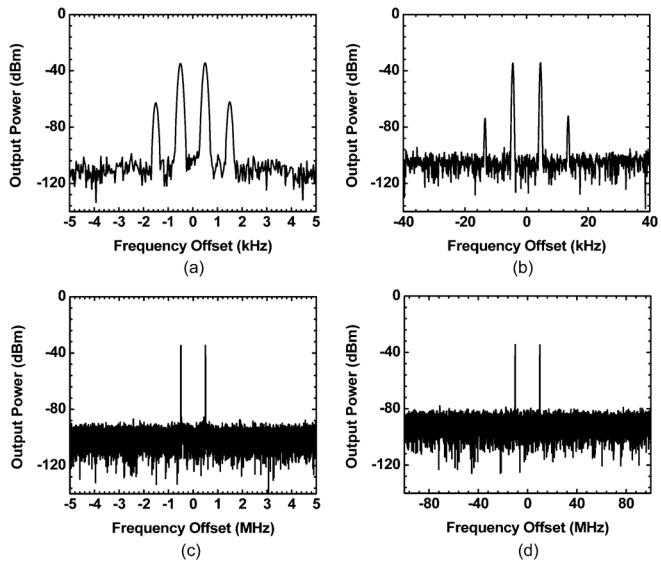

Fig. 17. Output spectrum with input offset of (a) 1 kHz; (b) 9 kHz; (c) 1 MHz; and (d) 20 MHz.

Two-tone measurements are also carried out to verify the inter-modulation outputs generated from the tunable filter. A two-tone input is applied at the center frequency of 5.25 GHz with input power of −10 dBm when the two-pole tunable notch filter is tuned to 5.25 GHz. The measured output spectra with frequency offset of 1 kHz, 9 kHz, 1 MHz, and 20 MHz are shown in Fig. 17(a)–(d). It can be found that intermodulation output terms are attenuated as the input frequency offset increases, which is consistent with the simulation results using the nonlinear RF MEMS model. The extracted third-order input intercept point (IIP_3) from the measurement is 10 dBm at 9 kHz frequency offset. The low mechanical Q of the membrane helps with avoiding linearity degradation when frequency offset is equal to the membrane natural resonance frequency. Significant linearity improvement can be obtained by using higher stiffness MEMS capacitor design or MEMS switched capacitors [41]. Although low bias voltage MEMS capacitor design is employed in this work, it is shown that the intermodulation terms generated due to the device nonlinearity do not cause additional interference across the whole UWB passband. These nonlinear analysis results show unique benefits of RF MEMS devices used in tunable bandstop filters.

C. Temperature Stability

The temperature stability of the fabricated micromachined filters are examined using a temperature-controlled probe station. The frequency response of the UWB filter is measured from to −30 °C to 70 °C. The frequency stability of the UWB passband edges are plotted in Fig. 18. It can be observed that the passband edges are very stable under the temperature change, and the rejection level of the filter is maintained.

A two-pole tunable notch filter is also characterized under temperature change (Fig. 19). The notch filter is tuned to 5.8 GHzf at room temperature. It can be seen that the measured center frequency drift is 5.6% when temperature is changed

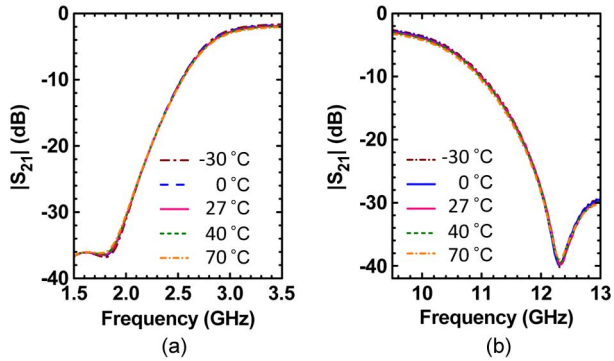

Fig. 18. Frequency stability of the UWB bandpass filter edges. (a) High-pass edge. (b) Low-pass edge.

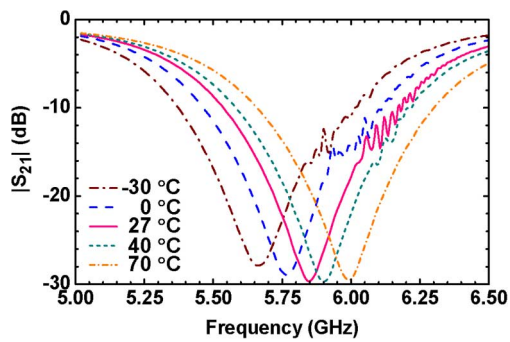

Fig. 19. Frequency responses of the two-pole tunable notch filter at different temperatures.

from −30 °C to 70 °C. The frequency shift because of temperature change is significantly smaller than the electrostatic frequency tuning range, which is more than 60% (Fig. 11). Therefore, frequency change due to temperature drift can be compensated by adjusting the bias on the tunable notch filter. Improvement to the temperature stability of the RF MEMS tunable notch filter can be achieved using a temperature-stable RF MEMS design [31].

V. Conclusion

In this paper, a silicon-based IPD technology is developed for the implementation of miniaturized UWB bandpass filters as well as tunable notch filters. Design and characterization of UWB bandpass filters and tunable notch filters are presented. The fabricated filters exhibit high performances on a silicon substrate, which makes them suitable candidates for highly integrated UWB RF front-end modules.

Acknowledgment

The authors would like to acknowledge the staff of the Lurie Nanofabrication Facility at the University of Michigan for their assistance with fabrication.

References

[1] FCC Code of Federal Register (CFR), Title 47, pt. 15, United States.
[2] P. P. Mercier, D. C. Daly, and A. P. Chandrakasan, “An energy-efficient all-digital UWB transmitter employing dual capacitively-coupled pulse-shaping drivers,” *IEEE J. Solid-State Circuits*, vol. 44, no. 6, pp. 1679–1688, Jun. 2009.
[3] Y. Park and D. D. Wentzloff, “An all-digital 12 pJ/pulse IR-UWB transmitter synthesized from a standard cell library,” *IEEE J. Solid-State Circuits*, vol. 46, no. 5, pp. 1147–1157, May 2011.

[4] F. S. Lee and A. P. Chandrakasan, "A 2.5 nJ/bit 0.65 V pulsed UWB receiver in 90 nm CMOS," *IEEE J. Solid-State Circuits*, vol. 42, no. 12, pp. 2851–2859, Dec. 2007.

[5] F. Zhang, A. Jha, R. Gharpurey, and P. Kinget, "An agile, ultra-wideband pulse radio transceiver with discrete-time wideband-IF," *IEEE J. Solid-State Circuits*, vol. 44, no. 5, pp. 1336–1351, May 2009.

[6] T. Kikkawa, P. K. Saha, N. Sasaki, and K. Kimoto, "Gaussian monocycle pulse transmitter using 0.18 μm CMOS technology with on-chip integrated antennas for inter-chip UWB communication," *IEEE J. Solid-State Circuits*, vol. 43, no. 5, pp. 1303–1312, May 2008.

[7] A. Vallese, A. Bevilacqua, C. Sandner, M. Tiebout, A. Gerosa, and A. Neviani, "Analysis and design of an integrated notch filter for the rejection of interference in UWB systems," *IEEE J. Solid-State Circuits*, vol. 44, no. 2, pp. 331–343, Feb. 2009.

[8] G. Cusmai, M. Brandolini, P. Rossi, and F. Svelto, "A 0.18- μm CMOS selective receiver front-end for UWB applications," *IEEE J. Solid-State Circuits*, vol. 41, no. 8, pp. 1764–1771, Aug. 2006.

[9] A. Medi and W. Namgoong, "A high data-rate energy-efficient interference-tolerant fully integrated CMOS frequency channelized UWB transceiver for impulse radio," *IEEE J. Solid-State Circuits*, vol. 43, no. 4, pp. 974–980, Apr. 2008.

[10] R. Roovers, D. M. W. Leenaerts, J. Bergervoet, K. S. Harish, R. C. H. van de Beek, G. van der Weide, H. Waite, Y. Zhang, S. Aggarwal, and C. Razzell, "An interference-robust receiver for ultra-wideband radio in SiGe BiCMOS technology," *IEEE J. Solid-State Circuits*, vol. 40, no. 12, pp. 2563–2572, Dec. 2005.

[11] T. Norimatsu, R. Fujiwara, M. Kokubo, M. Miyazaki, A. Maeki, Y. Ogata, S. Kobayashi, N. Koshizuka, and K. Sakamura, "A UWB-IR transmitter with digitally controlled pulse generator," *IEEE J. Solid-State Circuits*, vol. 42, no. 6, pp. 1300–1309, Jun. 2007.

[12] Z. C. Hao and J. S. Hong, "Ultrawideband filter technologies," *IEEE Microw. Mag.*, vol. 11, no. 4, pp. 56–68, Jun. 2010.

[13] H. Liang, K. Wu, and X. Zhang, "Development of packaged ultra-wideband bandpass filters," *IEEE Trans. Microw. Theory Tech.*, vol. 58, no. 1, pp. 220–228, Jan. 2010.

[14] Y. Chen, S. Chang, C. Wei, Y. Wang, and C. H. Huang, "Packaged ultra-wide-band bandpass filter based on inverted-T multiple-mode resonators and inverted-F impedance transformers," *IEEE Microw. Mag.*, vol. 11, no. 1, pp. 126–129, Feb. 2010.

[15] Z. C. Hao and J. S. Hong, "UWB bandpass filter Using cascaded miniature high-pass and low-pass filters with multilayer liquid crystal polymer technology," *IEEE Trans. Microw. Theory Tech.*, vol. 58, no. 4, pp. 941–948, Apr. 2010.

[16] H. Shamanand and J. S. Hong, "Ultra-wideband (UWB) bandpass filter with embedded band notch structures," *IEEE Microw. Wireless Compon. Lett.*, vol. 17, no. 3, pp. 193–195, Mar. 2007.

[17] Z. C. Hao and J. S. Hong, "Compact UWB filter with double notch-bands using multilayer LCP technology," *IEEE Microw. Wireless Compon. Lett.*, vol. 19, no. 8, pp. 500–502, Aug. 2009.

[18] X. Luo, J. G. Ma, K. S. Yeo, and E. P. Li, "Compact ultra-wideband (UWB) bandpass filter with ultra-narrow dual-and quad-notched bands," *IEEE Trans. Microw. Theory Tech.*, vol. 59, no. 6, pp. 1509–1519, Jun. 2011.

[19] H. R. Arachchige, J. S. Hong, and Z. C. Hao, "UWB bandpass filter with tunable notch on liquid crystal polymer substrate," in *Asia-Pacific Microw. Conf.*, Dec. 2008, pp. 1–4.

[20] Z. Wu, Y. Shim, and M. Rais-Zadeh, "Miniaturized UWB bandpass filters integrated with notch filters using a silicon-based integrated passive device technology," in *IEEE/MTT-S Int. Microw. Symp.*, Jun. 2011, pp. 1–4.

[21] W. D. Yan and R. R. Mansour, "Compact tunable bandstop filter integrated with large deflected actuators," in *IEEE/MTT-S Int. Microw. Symp.*, Jun. 2007, pp. 1611–1614.

[22] H. S. Lee, D. H. Choi, and J. B. Yoon, "MEMS-based tunable LC bandstop filter with an ultra-wide continuous tuning range," *IEEE Microw. Wireless Compon. Lett.*, vol. 19, no. 11, pp. 710–712, Nov. 2009.

[23] E. Lourandakis, M. Schmidt, S. Seitz, and R. Weigel, "Tunable lumped element filters with BST thin-film varactors," in *Eur. Microw. Conf.*, Oct. 2008, pp. 1691–1694.

[24] I. Reines, S. J. Park, and G. M. Rebeiz, "Compact low-loss tunable X-band bandstop filter with miniature RF-MEMS switches," *IEEE Trans. Microw. Theory Tech.*, vol. 58, no. 7, pp. 1887–1895, Jul. 2010.

[25] C. Musoll-Anguiano, I. Llamas-Garro, Z. Brito-Brito, L. Pradell, and A. Corona-Chavez, "Characterizing a tune all bandstop filter," in *IEEE/MTT-S Int. Microw. Workshop Series on Signal Integrity and High-Speed Interconnects*, Feb. 2009, pp. 55–58.

[26] Z. Brito-Brito, I. Llamas-Garro, L. Pradell-Cara, and A. Corona-Chavez, "Microstrip switchable bandstop filter using PIN diodes with precise frequency and bandwidth control," in *Eur. Microw. Conf.*, Oct. 2008, pp. 1707–1710.

[27] D. R. Jachowski and C. Rauscher, "Frequency-agile bandstop filter with tunable attenuation," in *IEEE/MTT-S Int. Microw. Symp. Digest*, Jun. 2009, pp. 649–652.

[28] B. Smilowitz, "High speed varactor tuned notch filter," in *IEEE/MTT-S Int. Microw. Symp. Digest*, June 1985, pp. 531–534.

[29] R. Gharpurey and P. Kinget, *Ultra Wideband: Circuits, Transceivers and Systems*. Boston, MA: Springer, 2008, pp. 60–61.

[30] T. G. S. M. Rijks *et al.*, "Micro-electro-mechanical tunable capacitors for reconfigurable RF architectures," *J. Micromech. Microeng.*, vol. 16, no. 3, pp. 601–611, Mar. 2006.

[31] Y. Shim, Z. Wu, and M. Rais-Zadeh, "A high-performance temperature-stable continuously tuned MEMS capacitor," in *IEEE Int. Conf. Microelectromech. Syst. (MEMS'11)*, Cancun, Mexico, 2011, pp. 752–755.

[32] C. D. Patel and G. M. Rebeiz, "An RF-MEMS switch with mN contact forces," in *IEEE/MTT-S Int. Microw. Symp. Digest*, May 2010, pp. 1242–1245.

[33] "HFSS 1". Ansoft Corporation, Pittsburgh, PA, 2009.

[34] J. D. Rhodes and S. A. Alseyab, "The generalized Chebyshev low-pass prototype filter," *Int. J. Circuit Theory Appl.*, vol. 8, no. 4, pp. 113–125, Apr. 1980.

[35] C. W. Tang and D. L. Yang, "Realization of multilayered wide-passband bandpass filter with low-temperature co-fired ceramic technology," *IEEE Trans. Microw. Theory Tech.*, vol. 56, no. 7, pp. 1668–1674, Jul. 2008.

[36] S. S. Mohan, C. P. Yue, M. del Mar Hershenson, S. S. Wong, and T. H. Lee, "Modeling and characterization of on-chip transformers," in *Int. Electron Devices Meeting*, Dec. 1998, pp. 531–534.

[37] B. M. Schiffman and G. L. Matthaei, "Exact design of band-stop microwave filters," *IEEE Trans. Microw. Theory Tech.*, vol. 12, no. 1, pp. 6–15, Jan. 1964.

[38] D. M. Pozar, *Microwave Engineering*. Hoboken, NJ: Wiley, 2005.

[39] J. Hogerheiden, M. Ciminera, and G. Jue, "Improved planar spiral transformer theory applied to a miniature lumped element quadrature hybrid," *IEEE Trans. Microw. Theory Tech.*, vol. 45, no. 4, pp. 543–545, Apr. 1997.

[40] A. Cruau, P. Nicole, G. Lissorgues, and C. M. Tassetti, "Influence of RF signal power on tunable MEMS capacitors," in *Eur. Microw. Conf.*, Oct. 2003, vol. 2, pp. 663–666.

[41] G. M. Rebeiz, *RF MEMS: Theory, Design, and Technology*. Hoboken, NJ: Wiley, 2003.

[42] L. Dussopt and G. M. Rebeiz, "Intermodulation distortion and power handling in RF MEMS switches, varactors, and tunable filters," *IEEE Trans. Microw. Theory Tech.*, vol. 51, no. 4, pp. 1247–1256, Apr. 2003.

[43] "Advanced Design System 2009A". Agilent Technol. Inc., Palo Alto, CA, 2009.

Zhengzheng Wu (S'09) received the B.S. degree in microelectronics from Fudan University, Shanghai, China, in 2005, and the M.S. degree in microelectronics from the Shanghai Institute of Microsystem and Information Technology, Chinese Academy of Sciences, Shanghai, China, in 2009. Currently, he is working towards the Ph.D. degree in electrical engineering and computer science at the University of Michigan, Ann Arbor.

During the summer of 2011, he was an Intern with Samsung Telecommunications America, Dallas, TX, where he was involved in developing multiband RF power amplifiers for wireless handsets. His research interests include MEMS for wireless applications and timing references, tunable RF filters and passive circuits, circuits for wireless transceivers, and integrated Microsystems.

Mr. Wu received the Rackham International Student Fellowship from the University of Michigan for 2010–2011. He was a student paper competition finalist at the 2011 International Microwave Symposium.

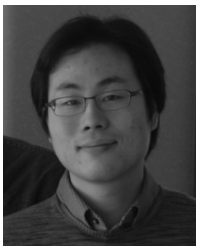

Yonghyun Shim (S'09) received the B.S. degree in electrical engineering from Seoul National University, Seoul, Korea, in 2007, and the M.S.E. degree in electrical engineering and computer science from the University of Michigan, Ann Arbor, in 2009. Currently, he is working towards the Ph.D. degree in electrical engineering and computer science at the University of Michigan, Ann Arbor.

His research interests include micromachined RF front-end filters, RF MEMS passives, RF IC and wireless front-end, and CMOS-MEMS integration.

Mina Rais-Zadeh (S'03–M'08) received the B.S. degree in electrical engineering from the Sharif University of Technology ,Tehran, Iran, and the M.S. and Ph.D. degrees in electrical and computer engineering from Georgia Institute of Technology, Atlanta, in 2005 and 2008, respectively.

From August 2008 to 2009, she was a Postdoctoral Research Fellow with the Integrated MEMS Group, Georgia Institute of Technology. Since January 2009, she has been with the University of Michigan, Ann Arbor, where she is currently an Assistant Professor in the Department of Electrical Engineering and Computer Science. Her research interests include passive micromachined devices for communication applications, resonant micromechanical devices, gallium nitride MEMS, and micro/nano fabrication process development.

Prof. Rais-Zadeh is the recipient of the NSF CAREER Award (2011), the IEEE Electron Device Society Early Career Award (2011), and finalist in the student paper competitions at the SiRF (2007) and IMS (2011) conferences. She serves as a member of the technical program committee of IEEE IEDM, IEEE Sensors, and Hilton Head workshop.